

## Modified radius-weighted lattice Boltzmann model to address singularities in axisymmetric multiphase flows

Xingchun Xu,<sup>1</sup> Yanwei Hu,<sup>2</sup> Yurong He,<sup>2</sup> Jiecai Han,<sup>1</sup> and Jiaqi Zhu<sup>1,3,\*</sup>

<sup>1</sup>National Key Laboratory of Science and Technology on Advanced Composites in Special Environments, Harbin Institute of Technology, Harbin 150080, China

<sup>2</sup>School of Energy Science & Engineering, Harbin Institute of Technology, Harbin 150001, China

<sup>3</sup>Key Laboratory of Micro-systems and Micro-structures Manufacturing, Ministry of Education, Harbin 150080, China



(Received 5 November 2021; revised 3 April 2022; accepted 2 August 2022; published 29 August 2022)

The radius-weighted lattice Boltzmann model has achieved great success in the simulation of axisymmetric flows. However, severe spurious currents near the axis are observed when this model is extended to simulate axisymmetric multiphase flows. In this study, to determine the origin of this singularity, we conducted a truncation error analysis based on high-order Taylor series expansion and identified the leading error terms through dimensionless analysis. By neglecting the error terms in proportion to the radius, we obtained the final forms of the singular terms in the axisymmetric lattice Boltzmann model. We proposed a modified model by including an additional correction term, to remove the singularity at the third order. We validated the proposed model using numerical tests for flat and spherical interfaces. Results showed that the present modified model reduced the spurious currents near the axis by two orders of magnitude compared with the original model. This modified model also has been successfully applied to predict bubble dynamics in an air-water system. Our numerical results are in excellent agreement with available experimental observations in terms of bubble shapes and terminal velocities.

DOI: [10.1103/PhysRevE.106.025316](https://doi.org/10.1103/PhysRevE.106.025316)

### I. INTRODUCTION

Axisymmetric models are widely used in science and engineering to simulate cylindrical flows. Compared with three-dimensional (3D) models, axisymmetric models bypass elaborate cylindrical boundary conditions and have lower computational costs. Recently, the lattice Boltzmann (LB) method has received increasing attention due to its mesoscopic and kinetic nature. However, standard LB models are developed within the Cartesian coordinate system, and additional treatment must be taken to obtain a consistent LB model for the axisymmetric case.

Existing axisymmetric LB models can be classified into two categories. The first is built within the pseudo-Cartesian coordinate system by adding virtual source terms, which is referred to as a top-down model. Early top-down models had complex source terms and required additional finite difference calculations to obtain velocity gradients [1–3]. Zhou [4] proposed a simplified axisymmetric LB model, in which fewer source terms were introduced but velocity gradients were maintained. Li *et al.* [5] proposed an efficient approach for recovering the velocity gradient term using the nonequilibrium part of the distribution function, which was further incorporated into the collision operator with a radius-dependent relaxation time. In a similar way, Zhou [6] removed the velocity gradient in his revised axisymmetric model; unlike the Li *et al.* [5] model, this revised model

applied semi-implicit centered schemes for the source terms so that macroscopic variables can be determined using the same formulas employed in the conventional two-dimensional (2D) LB model. In contrast, Guo *et al.* [7] developed a different type of axisymmetric LB model from the continuous Boltzmann equation in cylindrical coordinates; its most distinguishing feature was the adoption of a new distribution function that was multiplied by the radius, and thus this type of model is also referred to as the radius-weighted lattice Boltzmann (RW-LB) model. The main advantages of this model are that it solves axial, radial, and azimuthal velocity in a consistent manner, and that the source terms are simple without nonlocal velocity gradients. A comparative study of different axisymmetric LB models was conducted by Zhang *et al.* [8] and demonstrated the superior accuracy and computation time of the RW-LB model compared with Li *et al.* [5] model and Zhou's modified model [6]. The RW-LB model has been widely extended to various applications including the analysis of thermal flow [9], solid-liquid phase change [10], and multiphase flow [11,12].

Based on different physical background, various LB models for multiphase flow have been proposed, including the color-gradient method [13], pseudopotential method [14,15], free energy model [16,17], and phase field model [18–21]. One undesirable feature common to these models is the existence of spurious currents near the phase interface. A review of spurious currents in different lattice Boltzmann models for multiphase flow can be found in Ref. [22]. Theoretically, such an artificial velocity field arises from an imbalance between discretized forces in the interfacial region [23]. The magnitude

\*zhujq@hit.edu.cn

of the spurious current is related to the radius of the drop, surface tension, ratio of viscosity, and details of the method. These unphysical flows affect numerical stability, limit the density ratio, and reduce accuracy [13].

Many studies have attempted to reduce or eliminate these spurious currents using different approaches. Shan [14] reduced the spurious current in a pseudopotential-based model by increasing the isotropy of the discrete gradient operator. Leclaire *et al.* [13] adopted high-order isotropic color-gradient operators in a color gradient model to reduce spurious currents caused by standard anisotropic schemes by an order of magnitude. As for the free energy- or phase field-based models, the formulations of surface tension force and corresponding discrete schemes are essential factors influencing the formation of spurious currents. Swift *et al.* [16] first proposed a free energy-based lattice Boltzmann model for two-phase flows by introducing a pressure tensor in the equilibrium function. Seta and Okui [24] analyzed the truncation errors of the derivatives in the pressure tensor and found that applying fourth-order schemes reduced spurious currents by approximately one half of those obtained using second-order schemes. Pooley and Furtado [25] redesigned the pressure tensor by selecting the best stencils for the first derivative and Laplacian operator, which decreased spurious currents by an order of magnitude compared with the original models. Wagner [23] replaced the pressure tensor divergence with surface tension force in a potential form; although the spurious current was reduced, numerical instability occurred, necessitating the addition of a small amount of numerical viscosity to this model. Subsequently, Lee and Fischer [26] proposed a stable discretization scheme using the second-order mixed difference for the gradient terms. Guo *et al.* [27] analyzed force balance at the discrete level for a flat interface and demonstrated that a small imbalance force would inevitably produce artificial velocity in conventional LB models. Very recently, Guo [28] performed a further analysis of the discrete errors and developed a well-balanced LB model that could achieve the equilibrium state.

Despite these achievements, we note all pertain to 2D cases; few studies have examined spurious currents in the 2D axisymmetric model. From a theoretical perspective, axisymmetric models are often associated with complex or unique virtual source terms, making it much harder to realize force balance at the discrete level. As a result, larger spurious currents occur in the phase interface region. The consistency of the RW-LB model when extended to multiphase flow simulations also remains to be demonstrated. The use of radial coordinates in the distribution function and force term may modify the truncation error terms; the effect on model precision should be clearly stated. This study describes the phenomenon of a singularity in the RW-LB model, which produced large spurious currents near the axis. The objective of this study is to determine the origin of this singularity and develop a modified model to eliminate it. The remainder of this paper is organized as follows. In Sec. II the extension of the RW-LB model to the axisymmetric multiphase flow is reviewed; to guarantee mass conservation, we develop an alternative LB model for the axisymmetric Allen-Cahn equation. Then in the next section, the truncation errors of the RW-LB model are derived from the Taylor series expansion, and the third-order leading error terms are extracted based on

the dimensionless analysis. In Sec. IV we describe our development of a modified model to remove singular terms through the introduction of an additional discrete source term. Numerical tests are conducted in Sec. V to demonstrate the capability of the proposed model to reduce spurious currents. Also, we simulated the single rising bubble driven by buoyancy force to check the validity of our model in capturing realistic phase interfaces. Finally, a brief summary is presented in Sec. VI.

## II. METHODOLOGY

### A. Macroscopic governing equations

The method of combining phase field and Navier-Stokes equations has been widely applied in multiphase flow simulations. For the axisymmetric case, the conservative Allen-Cahn equation in pseudo-Cartesian coordinates  $(r, z)$  can be written as [12]

$$\partial_t \phi + \partial_\alpha (\phi u_\alpha) + \frac{\phi u_r}{r} = \partial_\alpha [M_\phi (\partial_\alpha \phi - \theta n_\alpha)] + \frac{M_\phi}{r} (\partial_r \phi - \theta n_r), \quad (1)$$

where Greek letter subscripts take their possible values from  $[r, z]$  and follow the Einstein summation convention.  $M_\phi$  is the mobility parameter and  $\phi$  is the order parameter, which takes a value of  $\phi_h$  and  $\phi_l$  for the heavy and light phases, respectively. The phase interface is determined by  $\phi_0 = (\phi_h + \phi_l)/2$ . The unit vector normal to the interface can be expressed as  $\mathbf{n} = \frac{\nabla \phi}{|\nabla \phi|}$  with  $\nabla \phi = (\partial_r \phi, \partial_z \phi)$ .  $\theta$  is the magnitude of phase field gradient at equilibrium,  $\theta = |\nabla \phi^{\text{eq}}|$ . The phase field at equilibrium exhibits a hyperbolic tangent profile,

$$\phi^{\text{eq}}(\xi) = \frac{\phi_h + \phi_l}{2} + \frac{\phi_h - \phi_l}{2} \tanh\left(\frac{2\xi}{W}\right), \quad (2)$$

where  $W$  is the interface width, the coordinate axis  $\xi$  is normal to the interface, and  $\xi = 0$  is located at the phase interface. Following Eq. (2), we have  $\theta = \left| \frac{d\phi^{\text{eq}}}{d\xi} \right| = \frac{4(\phi_h - \phi_l)(\phi_h - \phi_l)}{W(\phi_h - \phi_l)}$ .

The chemical potential  $\mu_\phi$  is defined as

$$\mu_\phi = 4\beta(\phi - \phi_l)(\phi - \phi_h)(\phi - \phi_0) - \kappa(\partial_\beta \beta \phi + \partial_r \phi / r), \quad (3)$$

where coefficients  $\beta$  and  $\kappa$  are related to the surface tension  $\sigma$  and interface width  $W$  according to  $\beta = \frac{12\sigma}{|\phi_h - \phi_l|^4 W}$  and  $\kappa = \frac{3}{2|\phi_h - \phi_l|^2} W \sigma$ . It is important to note that the formulas for  $\theta$ ,  $\beta$ , and  $\kappa$  provided in a previous study [29] apply only to the case of  $\phi_h = 1$  and  $\phi_l = 0$ .

The Navier-Stokes equations are expressed in a form corresponding to the recovered macroscopic equation for the axisymmetric RW-LB model [12]:

$$\begin{aligned} \partial_\beta (r u_\beta) &= 0, \\ r \rho (\partial_t u_\alpha + u_\beta \partial_\beta u_\alpha) &= -\partial_\alpha (r p) + \partial_\beta [r v \rho (\partial_\beta u_\alpha + \partial_\alpha u_\beta)] \\ &\quad + r (F_{b\alpha} + F_{s\alpha}) + \left( p - \frac{2\rho v}{r} u_r \right) \delta_{\alpha r}, \end{aligned} \quad (4a)$$

where  $\rho$ ,  $p$ , and  $v$  are the density, pressure, and kinematic viscosity, respectively.  $\mathbf{F}_b$  is the body force. The surface tension

force  $F_s$  can be expressed in different continuous formulations [30]. In this study, we adopted the form of  $F_s = \mu_\phi \nabla \phi$ , which is simple and involves only the nonlocal expressions of  $\partial_\alpha \phi$  and  $\partial_{\beta\beta} \phi$ .

### B. The LB model for the Allen-Cahn equation

For the axisymmetric Allen-Cahn equation, Liang *et al.* [12] proposed a radius-weighted lattice Boltzmann model; however, this model lacks mass conservation for rough meshes, even without flow [29]. To avoid this problem, we omitted the last term in Eq. (1), which is feasible because the phase field remains in a quasi-equilibrium state during its convective motion, such that this term  $M_\phi(\partial_r \phi - \theta n_r)/r$  theoretically equals zero. The LB evolution equation for the order parameter can be expressed as

$$h_i(\mathbf{x} + \mathbf{e}_i \delta_t, t + \delta_t) - h_i(\mathbf{x}, t) = -\frac{h_i(\mathbf{x}, t) - h_i^{\text{eq}}(\mathbf{x}, t)}{\tau_m} + \left(1 - \frac{1}{2\tau_m}\right) \delta_t H_i(\mathbf{x}, t), \quad (5)$$

where the relaxation time  $\tau_m$  is related to the mobility by  $M_\phi = (\tau_m - 0.5)c_s^2 \delta_t$ . For the D2Q9 lattice model, the sound speed is defined as  $c_s = c/\sqrt{3}$ , where  $c$  is the ratio of lattice length  $\delta_x$  and time step  $\delta_t$ . The equilibrium distribution is given by

$$h_i^{\text{eq}} = w_i \phi + \phi s_i(\mathbf{u}) \quad (6)$$

with

$$s_i(\mathbf{u}) = w_i \left[ \frac{\mathbf{e}_i \cdot \mathbf{u}}{c_s^2} + \frac{(\mathbf{e}_i \cdot \mathbf{u})^2}{2c_s^4} - \frac{\mathbf{u} \cdot \mathbf{u}}{2c_s^2} \right]. \quad (7)$$

The lattice vectors  $\mathbf{e}_i = (e_{ir}, e_{iz})$  are defined as

$$\mathbf{e} = \begin{bmatrix} 0 & 1 & 0 & -1 & 0 & 1 & -1 & -1 & 1 \\ 0 & 0 & 1 & 0 & -1 & 1 & 1 & -1 & -1 \end{bmatrix} c, \quad (8)$$

and the weighting coefficients for the lattice vectors are given by  $w_0 = 4/9$ ,  $w_{1-4} = 1/9$ , and  $w_{5-8} = 1/36$ . To recover the macroscopic equation, the source term  $H_i$  is given by

$$H_i = w_i e_{i\alpha} \theta n_\alpha - w_i \frac{\phi u_r}{r}. \quad (9)$$

The macroscopic order parameter can be calculated by

$$\phi = \frac{\sum_i h_i}{1 + 0.5 \delta_t u_r / r} \quad (10)$$

and the density  $\rho$  can be calculated by linear interpolation of the densities for the light phase ( $\rho_l$ ) and heavy phase ( $\rho_h$ ), as follows:

$$\rho = \frac{\phi - \phi_l}{\phi_h - \phi_l} (\rho_h - \rho_l) + \rho_l. \quad (11)$$

The present Allen-Cahn equation-based axisymmetric LB model is similar to that one for 2D case [31,32]. A subtle difference is the additional term involved  $u_r/r$  in Eqs. (9) and (10). When the velocity is zero everywhere, both models are identical such that the mass conservation can be guaranteed in our axisymmetric model in the same manner as a 2D model. As the convection process is considered, theoretical analysis and numerical validation of the present model are presented in the Appendix A and B, respectively.

### C. The RW-LB model for hydrodynamics

In this section we recall the RW-LB model for axisymmetric multiphase flow proposed by Liang *et al.* [11]. The evolution equation for the axisymmetric fluid flow can be written as

$$f_i(\mathbf{x} + \mathbf{e}_i \delta_t, t + \delta_t) - f_i(\mathbf{x}, t) = -\frac{f_i - f_i^{\text{eq}}}{\tau} + \delta_t \left(1 - \frac{1}{2\tau}\right) R_i, \quad (12)$$

where the relaxation factor  $\tau$  is related to viscosity through  $\nu = (\tau - 0.5)c_s^2 \delta_t$ . The viscosity in the interface region can be obtained through the harmonic interpolation [33]:

$$\frac{1}{\tau} = \frac{1}{\tau_l} + \frac{\phi - \phi_l}{\phi_h - \phi_l} \left( \frac{1}{\tau_h} - \frac{1}{\tau_l} \right). \quad (13)$$

The equilibrium state of the particle distribution function  $f_i$  is defined as

$$f_i^{\text{eq}} = r \left( w_i \frac{p}{c_s^2} + \rho s_i(\mathbf{u}) \right). \quad (14)$$

The source term is designed as

$$R_i = \frac{(e_{i\alpha} - u_\alpha) \{ r s_i(\mathbf{u}) \partial_\alpha (\rho c_s^2) + r F_\alpha [w_i + s_i(\mathbf{u})] \}}{c_s^2} + \frac{w_i u_\alpha (\rho c_s^2 - p) \delta_{\beta r} (c_{i\alpha} c_{i\beta} - c_s^2 \delta_{\alpha\beta})}{c_s^4}, \quad (15)$$

where the equivalent total force is  $F_\alpha = F_{s\alpha} + F_{b\alpha} + \frac{rp - 2\rho\nu u_r}{r^2} \delta_{\alpha r}$ . Following high-order expansion on  $\delta_t$ ,  $F_\alpha$  consists of two different orders:  $F_\alpha = F_{0\alpha} + \delta_t F_{1\alpha}$ , where  $F_{0\alpha} = F_{s\alpha} + F_{b\alpha} + \frac{p}{r} \delta_{\alpha r}$  and  $F_{1\alpha} = -\frac{2\rho(\tau - 0.5)c_s^2 u_r}{r^2} \delta_{\alpha r}$ .

The macroscopic pressure is obtained from the distribution function by

$$p = \frac{c_s^2}{r} \sum f_i + \frac{c_s^2 \delta_t}{2} u_\alpha \partial_\alpha \rho, \quad (16)$$

and the fluid velocity is

$$u_\alpha = \frac{\sum e_{i\alpha} f_i}{r\rho} + \frac{\delta_t}{2\rho} F_\alpha, \quad (17)$$

which can be rewritten explicitly as [12]

$$u_\alpha = \frac{\sum_i e_{i\alpha} f_i + 0.5 \delta_t r F_{0\alpha}}{r\rho + \delta_t r^{-1} \nu \rho \delta_{\alpha r}}. \quad (18)$$

The isotropic schemes of the spatial derivatives involved in the collision process and velocity calculation can be calculated as

$$\nabla \phi = \frac{1}{c_s^2 \delta_t} \sum_i e_i w_i \phi(\mathbf{x} + \mathbf{e}_i \delta_t, t) \quad (19)$$

and

$$\nabla^2 \phi = \partial_{\beta\beta} \phi = \frac{2}{c_s^2 \delta_t^2} \sum_i w_i [\phi(\mathbf{x} + \mathbf{e}_i \delta_t, t) - \phi(\mathbf{x}, t)]. \quad (20)$$

These expressions for the RW-LB model presented have been slightly simplified. The equilibrium distribution function

in Eq. (14) is expressed in a unified compact form, whereas in the model of Liang *et al.* [11] the equilibrium distribution function at rest ( $i = 0$ ) is distinguished from those in other directions. As a result, the expression used to update the hydrodynamic pressure in Eq. (16) is simpler than that given by Liang *et al.* [11]. It should be pointed out that this modification has no effect on third-order truncation errors. In other words, the singularity emerged in the RW-LB model cannot be removed by adjusting the equilibrium distribution function at rest ( $f_0^{\text{eq}}$ ).

### III. THIRD-ORDER TRUNCATION ERROR ANALYSIS

Following the truncation error analysis of Holdych *et al.* [34], we analyzed the RW-LB model for multiphase flow up to the third order. By shifting the time continuum by  $-\delta_t$ , Eq. (12) can be recast in the following form:

$$\begin{aligned} f_i(\mathbf{x}, t) &= \left(1 - \frac{1}{\tau}\right) f_i(\mathbf{x} - \mathbf{e}_i \delta_t, t - \delta_t) \\ &+ \frac{1}{\tau} f_i^{\text{eq}}(\mathbf{x} - \mathbf{e}_i \delta_t, t - \delta_t) \\ &+ \delta_t \left(1 - \frac{1}{2\tau}\right) R_i(\mathbf{x} - \mathbf{e}_i \delta_t, t - \delta_t). \end{aligned} \quad (21)$$

With the recursive application of such an expression over an infinite number of time steps, the distribution function  $f_i$  is obtained from the equilibrium function  $f_i^{\text{eq}}(\mathbf{x} - n\mathbf{e}_i \delta_t, t - n\delta_t)$  and source term  $R_i(\mathbf{x} - n\mathbf{e}_i \delta_t, t - n\delta_t)$  as follows:

$$\begin{aligned} f_i &= \frac{1}{\tau} \sum_{n=1}^{\infty} \left(1 - \frac{1}{\tau}\right)^{n-1} f_i^{\text{eq}}(\mathbf{x} - n\mathbf{e}_i \delta_t, t - n\delta_t) \\ &+ \delta_t \left(1 - \frac{1}{2\tau}\right) \sum_{n=1}^{\infty} \left(1 - \frac{1}{\tau}\right)^{n-1} R_i(\mathbf{x} - n\mathbf{e}_i \delta_t, t - n\delta_t). \end{aligned} \quad (22)$$

Using the Taylor series expansion gives

$$\begin{aligned} f_i &= f_i^{\text{eq}} + \tau \sum_{m=1}^{\infty} \frac{p[\tau, m]}{m!} (\delta_t D_i)^m f_i^{\text{eq}} \\ &+ \delta_t \frac{2\tau - 1}{2} R_i + \delta_t \frac{2\tau - 1}{2} \tau \sum_{m=1}^{\infty} \frac{p[\tau, m]}{m!} (\delta_t D_i)^m R_i, \end{aligned} \quad (23)$$

where  $D_i = \partial_t + e_{i\alpha} \partial_\alpha$  and  $p[\tau, m]$  is defined as

$$p[\tau, m] = \frac{1}{\tau^2} \sum_{n=1}^{\infty} \left(1 - \frac{1}{\tau}\right)^{n-1} (-n)^m. \quad (24)$$

For  $m = 0, 1, 2, 3$ , we have [35]

$$\begin{aligned} p[\tau, 0] &= 1/\tau, \quad p[\tau, 1] = -1, \\ p[\tau, 2] &= 2\tau - 1, \quad p[\tau, 3] = -6\tau^2 + 6\tau - 1. \end{aligned} \quad (25)$$

For convenience of the high-order truncation error analysis, the zeroth and first velocity moments of the distribution function and source terms are obtained as follows:

$$\begin{aligned} \sum_i f_i &= \frac{r\rho}{c_s^2} - \frac{\delta_t}{2} r u_\alpha \partial_\alpha \rho, \\ \sum_i f_i^{\text{eq}} &= \frac{r\rho}{c_s^2}, \quad \sum_i R_i = r u_\alpha \partial_\alpha \rho, \end{aligned} \quad (26a)$$

$$\begin{aligned} \sum_i e_{i\alpha} f_i &= \rho r u_\alpha - \frac{\delta_t}{2} r F_\alpha, \\ \sum_i e_{i\alpha} f_i^{\text{eq}} &= \rho r u_\alpha, \quad \sum_i e_{i\alpha} R_i = r F_\alpha. \end{aligned} \quad (26b)$$

High-order moments of equilibrium equation and source term are expressed as  $\Pi_{\alpha\beta}^0 = \sum_i e_{i\alpha} e_{i\beta} f_i^{\text{eq}}$ ,  $\mathcal{Q}_{\alpha\beta\gamma}^0 = \sum_i e_{i\alpha} e_{i\beta} e_{i\gamma} f_i^{\text{eq}}$ ,  $A_{\alpha\beta\gamma\delta}^0 = \sum_i e_{i\alpha} e_{i\beta} e_{i\gamma} e_{i\delta} f_i^{\text{eq}}$ ,  $\Psi_{\alpha\beta} = \sum_i e_{i\alpha} e_{i\beta} R_i$ , and  $\Xi_{\alpha\beta\gamma} = \sum_i e_{i\alpha} e_{i\beta} e_{i\gamma} R_i$ . The zeroth and first velocity moments of Eq. (23) form the continuity equation

$$\begin{aligned} \frac{r}{c_s^2} \partial_t p + \partial_\alpha (\rho r u_\alpha) &= r u_\alpha \partial_\alpha \rho + (\tau - 0.5) \delta_t \left[ \frac{r}{c_s^2} \partial_{tt} p + 2 \partial_{t\alpha} (\rho r u_\alpha) + \partial_{\alpha\beta} \Pi_{\alpha\beta}^0 - \partial_t (r u_\alpha \partial_\alpha \rho) - \partial_\alpha (r F_\alpha) \right] \\ &+ \left( -\tau^2 + \tau - \frac{1}{6} \right) \delta_t^2 \left[ \frac{r}{c_s^2} \partial_{ttt} p + 3 \partial_{tt\alpha} (\rho r u_\alpha) + 3 \partial_{t\alpha\beta} \Pi_{\alpha\beta}^0 + \partial_{\alpha\beta\gamma} \mathcal{Q}_{\alpha\beta\gamma}^0 \right] \\ &+ \left( \tau - \frac{1}{2} \right)^2 \delta_t^2 [\partial_{tt} (r u_\alpha \partial_\alpha \rho) + 2 \partial_{t\alpha} (r F_\alpha) + \partial_{\alpha\beta} \Psi_{\alpha\beta}] + O(\delta_t^3) \end{aligned} \quad (27)$$

and momentum equation

$$\begin{aligned} \partial_t (\rho r u_\alpha) + \partial_\beta \Pi_{\beta\alpha}^0 &= r F_\alpha + (\tau - 0.5) \delta_t [\partial_{tt} (\rho r u_\alpha) + 2 \partial_{t\beta} \Pi_{\beta\alpha}^0 + \partial_{\beta\gamma} \mathcal{Q}_{\beta\gamma\alpha}^0 - \partial_t (r F_\alpha) - \partial_\beta \Psi_{\beta\alpha}] \\ &+ \left( -\tau^2 + \tau - \frac{1}{6} \right) \delta_t^2 [\partial_{ttt} (\rho r u_\alpha) + 3 \partial_{tt\beta} \Pi_{\beta\alpha}^0 + 3 \partial_{t\beta\gamma} \mathcal{Q}_{\beta\gamma\alpha}^0 + \partial_{\beta\gamma\delta} A_{\beta\gamma\delta\alpha}^0] \\ &+ \left( \tau - \frac{1}{2} \right)^2 \delta_t^2 [\partial_{tt} (r F_\alpha) + 2 \partial_{t\beta} \Psi_{\beta\alpha} + \partial_{\beta\gamma} \Xi_{\beta\gamma\alpha}] + O(\delta_t^3). \end{aligned} \quad (28)$$

The momentum equation is then used recursively for the second and third lines in Eq. (28). Retaining the terms up to  $O(\delta_t^2)$ , we have

$$\begin{aligned} \partial_t(\rho r u_\alpha) + \partial_\beta \Pi_{\beta\alpha}^0 &= r F_\alpha + (\tau - 0.5)\delta_t \partial_\beta (\partial_t \Pi_{\alpha\beta}^0 + \partial_\gamma Q_{\beta\gamma\alpha}^0 - \Psi_{\beta\alpha}) \\ &+ \left(-\tau^2 + \tau - \frac{1}{12}\right)\delta_t^2 \partial_{t\beta} \Pi_{\beta\alpha}^0 + \left(-2\tau^2 + 2\tau - \frac{1}{4}\right)\delta_t^2 \partial_{t\beta\gamma} Q_{\beta\gamma\alpha}^0 \\ &+ \left(-\tau^2 + \tau - \frac{1}{6}\right)\delta_t^2 \partial_{\beta\gamma\delta} A_{\beta\gamma\delta\alpha}^0 + \left(\tau - \frac{1}{2}\right)^2 \delta_t^2 (\partial_{t\beta} \Psi_{\beta\alpha} + \partial_{\beta\gamma} \Xi_{\beta\gamma\alpha}) + \frac{1}{12}\delta_t^2 \partial_{tt} (r F_{0\alpha}) + O(\delta_t^3). \end{aligned} \quad (29)$$

Recall that  $F_\alpha = F_{0\alpha} + \delta_t F_{1\alpha}$ , and thus only  $F_{0\alpha}$  is retained in the last term. In Eq. (29) the first line corresponds to the recovered macroscopic equation up to the second-order expansion, where the terms in brackets can be expressed as

$$\partial_t \Pi_{\alpha\beta}^0 + \partial_\gamma Q_{\gamma\alpha\beta}^0 - \Psi_{\alpha\beta} = r \rho c_s^2 (\partial_\alpha u_\beta + \partial_\beta u_\alpha). \quad (30)$$

Similarly, using Eq. (29) and recursive substitution of Eq. (27), the continuum equation can be simplified as

$$\begin{aligned} \frac{r}{c_s^2} \partial_t p + \rho \partial_\alpha (r u_\alpha) &= \frac{\delta_t^2}{12} [\partial_{t\alpha\beta} \Pi_{\alpha\beta}^0 + \partial_{\alpha\beta\gamma} Q_{\alpha\beta\gamma}^0 + \partial_{tt} (r u_\alpha \partial_\alpha \rho) \\ &+ 2\partial_{t\alpha} (r F_{0\alpha})] + O(\delta_t^3). \end{aligned} \quad (31)$$

We applied dimensional analysis to identify the leading error terms of Eq. (29) at the third order. The scales for length and velocity are  $L$  and  $U$ , respectively. The normalized variables are obtained as

$$\bar{r} = r/L, \bar{u} = u/U, \bar{t} = tU/L, \bar{p} = p/\rho c_s^2, \bar{F}_\alpha = F_\alpha L/(\rho c_s^2). \quad (32)$$

Dropping the bar for simplicity, the nondimensional form of the recovered equation can be written as

$$\begin{aligned} \text{Ma}^2 r (\partial_t u_\alpha + u_\beta \partial_\beta u_\alpha) \\ = -\partial_\alpha (r p) + r F_{0\alpha} + \text{KnMa} \left[ \partial_\beta (r \partial_\beta u_\alpha + r \partial_\alpha u_\beta) - 2 \frac{u_r}{r} \delta_{\alpha r} \right] \\ + E_\alpha, \end{aligned} \quad (33)$$

where the Mach number  $\text{Ma} = U/c_s$  and Knudsen number  $\text{Kn} = c_s(\tau - 0.5)\delta_t/L$  are related to the Reynolds number  $\text{Re} = LU/\nu$  by  $\text{Ma} = \text{ReKn}$ . Among the third-order terms included in  $E_\alpha$ , the terms  $\partial_{t\beta} \Pi_{\beta\alpha}^0$ ,  $\partial_{t\beta\gamma} Q_{\beta\gamma\alpha}^0$ ,  $\partial_{t\beta} \Psi_{\beta\alpha}$ , and  $\partial_{tt} (r F_{0\alpha})$  are on the order of  $\text{Kn}^2 \text{Ma}^2$  and can be neglected by assuming  $\text{Ma} \ll 1$  and  $\text{Kn} < 1$ . The remaining terms,  $\partial_{\beta\gamma\delta} A_{\beta\gamma\delta\alpha}^0$  and  $\partial_{\beta\gamma} \Xi_{\beta\gamma\alpha}$ , are on the order of  $\text{Kn}^2$  and can be

expressed explicitly as

$$\partial_{\beta\gamma\delta} A_{\beta\gamma\delta\alpha}^0 = c_s^2 \partial_\beta [\partial_{\gamma\gamma} (r p) \delta_{\alpha\beta} + \partial_{\alpha\beta} (r p) + \partial_{\beta\alpha} (r p)], \quad (34a)$$

$$\begin{aligned} \partial_{\beta\gamma} \Xi_{\beta\gamma\alpha} &= c_s^2 \partial_\beta [\partial_\gamma (r F_{0\gamma}) \delta_{\alpha\beta} + \partial_\alpha (r F_{0\beta}) + \partial_\beta (r F_{0\alpha})] \\ &+ O(\delta_t). \end{aligned} \quad (34b)$$

Using the relationship

$$-\partial_\alpha (r p) + r F_{0\alpha} = O(\text{Ma}^2, \text{KnMa}) \quad (35)$$

gives

$$\begin{aligned} E_\alpha &= \frac{1}{12} \text{Kn}^2 \partial_\beta [\partial_\gamma (r F_{0\gamma}) \delta_{\alpha\beta} + \partial_\alpha (r F_{0\beta}) + \partial_\beta (r F_{0\alpha})] \\ &+ O(\text{Kn}^2 \text{Ma}^2, \text{Kn}^3 \text{Ma}). \end{aligned} \quad (36)$$

Thus, the final form of the recovered equation involved the leading error term up to the third order is

$$\begin{aligned} r \rho (\partial_t u_\alpha + u_\beta \partial_\beta u_\alpha) &= -\partial_\alpha (r p) + r F_{0\alpha} \\ &+ \partial_\beta [r \nu \rho (\partial_\beta u_\alpha + \partial_\alpha u_\beta)] \\ &- 2 \rho \nu u_r / r \delta_{\alpha r} + E_\alpha \end{aligned} \quad (37)$$

with the error term given by

$$E_\alpha = \frac{1}{12} \delta_t^2 c_s^2 \partial_\beta [\partial_\gamma (r F_{0\gamma}) \delta_{\alpha\beta} + \partial_\alpha (r F_{0\beta}) + \partial_\beta (r F_{0\alpha})]. \quad (38)$$

These error terms at the third order can also be derived through high-order Chapman-Enskog expansion [36]. Generally,  $E_\alpha$  is a high-order small quantity, which can be ignored in the 2D and 3D cases. However, in the axisymmetric RW-LB model for the multiphase flow, these error terms show a singularity near the axis of symmetry, which will produce large spurious currents. In the next section, we analyze these error terms and take measures to reduce the spurious currents caused by the singularity.

#### IV. MODIFIED RW-LB MODEL TO REMOVE SINGULARITY

One way to directly remove the error term  $E_\alpha$  is to add an additional source term in the evolution equation. Assuming that the additional source term takes the form of  $(1 - \frac{1}{2\tau})\delta_t R'_i$ , its moments should satisfy the following relationships:

$$\sum_i R'_i = 0, \quad \sum_i e_{i\alpha} R'_i = 0, \quad \sum_i e_{i\alpha} e_{i\beta} e_{i\gamma} R'_i = \Xi'_{\alpha\beta\gamma} = 0, \quad (39a)$$

$$\sum_i e_{i\alpha} e_{i\beta} R'_i = \Psi'_{\alpha\beta} = \frac{1}{12(\tau - 0.5)} \delta_t c_s^2 [\partial_\gamma (r F_{0\gamma}) \delta_{\alpha\beta} + \partial_\alpha (r F_{0\beta}) + \partial_\beta (r F_{0\alpha})]. \quad (39b)$$



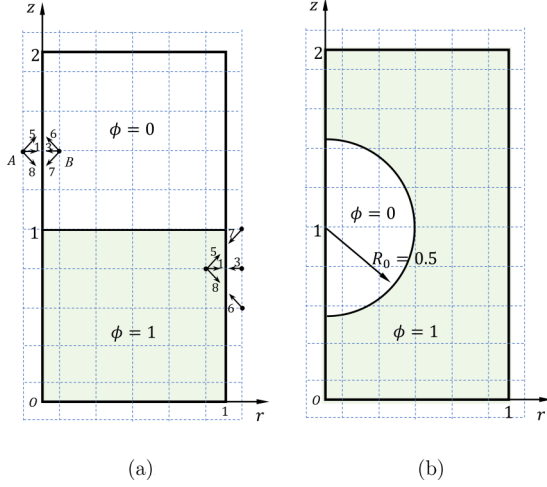


FIG. 1. Schematic diagrams for tests of spurious currents near (a) flat and (b) spherical interfaces.

Thus, the additional source term can be designed as

$$\left(1 - \frac{1}{2\tau}\right) \delta_t R'_i = \frac{\bar{w}_i}{12\tau} \delta_t^2 \frac{e_{i\alpha} e_{i\beta} \partial_\alpha (r F_{0\beta})}{c_s^2}, \quad (40)$$

where  $\bar{w}_0 = -\frac{5}{9}$  and  $\bar{w}_0 = w_0$ . Following similar high-order analysis as Sec. III, we obtain the correct macroscopic equation without the leading error terms at the third order. Spatial derivatives in Eq. (40) complicate the algorithm. When we incorporated Eq. (40) into the LB model, the singularity of spurious currents cannot be removed. Instead, the region of spurious currents was increased, which is unsurprising because the difference schemes introduced additional discretization errors.

To examine the origins of the singularity in Eq. (38) in greater detail, the force terms  $F_{0\alpha}$  are divided into two parts, i.e.,  $F_{0\alpha} = \hat{F}_{0\alpha} + p\delta_{\alpha r}/r$ , where the first part is independent of the radius and the second part produces a singularity at the axis. As well, we have the following relationships:

$$\begin{aligned} & \partial_\beta [\partial_\gamma (r \hat{F}_{0\gamma}) \delta_{\alpha\beta} + \partial_\alpha (r \hat{F}_{0\beta}) + \partial_\beta (r \hat{F}_{0\alpha})] \\ &= r(\partial_{\alpha\gamma} \hat{F}_{0\gamma} + \partial_{\alpha\beta} \hat{F}_{0\beta} + \partial_{\beta\beta} \hat{F}_{0\alpha}) \\ &+ 2\partial_\beta (\hat{F}_{0\alpha} \delta_{\beta r} + \hat{F}_{0\beta} \delta_{\alpha r} + \hat{F}_{0r} \delta_{\alpha\beta}). \end{aligned} \quad (41)$$

Two types of error term are included in these expressions: one that is proportional to  $r$  and one that is the first derivative of the force terms. Dividing both sides of Eq. (37) by  $r$ , the first type of error term shows no increasing trend near the axis, whereas the second type of error term causes a singularity at  $r = 0$ . By neglecting error terms that are proportional to  $r$ , Eq. (38) can be reorganized as

$$E_\alpha = \frac{1}{4} \delta_t^2 c_s^2 \partial_\beta (\hat{F}_{0\alpha} \delta_{\beta r} + \hat{F}_{0\beta} \delta_{\alpha r} + \hat{F}_{0r} \delta_{\alpha\beta}), \quad (42)$$

where we adopt the relationship  $-\partial_\alpha p + \hat{F}_{0\alpha} = 0$ , which is valid at the third order. These expressions show that the singularity depends on grid resolution and smooth force in the interface region.

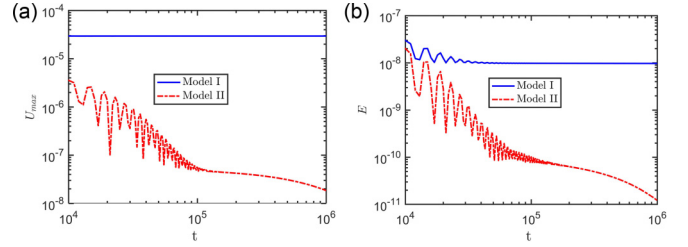


FIG. 2. Time history of (a) maximum magnitude of velocity ( $U_{\max}$ ) and (b) kinetic energy ( $E$ ) obtained by models I and II.

To remove the error terms in Eq. (42), we introduce an additional source term as

$$\left(1 - \frac{1}{2\tau}\right) \delta_t R'_i = \frac{\bar{w}_i}{4\tau} \delta_t^2 \frac{e_{i\alpha} e_{i\beta} (\hat{F}_{0\alpha} \delta_{\beta r})}{c_s^2}. \quad (43)$$

Compared with Eq. (40), Eq. (43) is simpler and can be conducted locally. The inclusion of this correction term allows us to remove the singularity caused by error terms at the third order. We summarize the modified model as follows:

$$\begin{aligned} & f_i(\mathbf{x} + \mathbf{e}_i \delta_t, t + \delta_t) - f_i(\mathbf{x}, t) \\ &= -\frac{f_i - f_i^{\text{eq}}}{\tau} + \delta_t \left(1 - \frac{1}{2\tau}\right) R_i + R_i^{\text{add}}, \end{aligned} \quad (44)$$

where the additional source term is

$$R_i^{\text{add}} = \frac{\bar{w}_i}{4\tau} \delta_t^2 \frac{e_{ir} e_{i\alpha} \hat{F}_{0\alpha}}{c_s^2}, \quad (45)$$

where  $\hat{F}_{0\alpha} = F_{s\alpha} + F_{b\alpha}$ . The equilibrium function  $f_i^{\text{eq}}$  and source term  $R_i$  are identical to those in the original model, as shown in Eqs. (14) and (15), respectively. For a static bubble without external body force, the singularity is produced by the surface tension force,  $F_s$ . As the gravitational force ( $F_b$ ) considered, it also produces a singularity due to the nonzero gradients near the interface.

## V. RESULTS AND DISCUSSION

In this section we validate the proposed model based on tests of static interfaces and a single rising bubble. The original RW-LB model and our modified one are referred to as models I and II, respectively. A comparative study is conducted on their performances of reducing spurious currents. Here we consider static flat and spherical interfaces in a cylinder, as shown in Fig. 1. The lateral walls are enforced by the half-way bounce-back conditions. The top and bottom

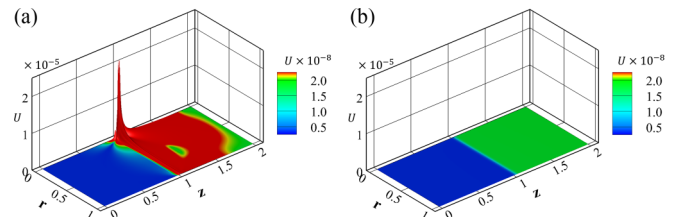
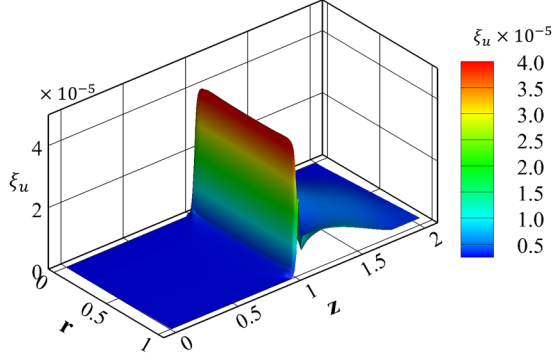


FIG. 3. Contours of spurious currents for a flat interface obtained by (a) model I and (b) model II.


 FIG. 4. Contour for the values of  $\xi_u = rN_R U$  in model I.

walls are periodic. In the RW-LB model, the axis boundary conditions cannot be directly treated at  $r = 0$ . Guo *et al.* [7] proposed a symmetric scheme by setting the symmetry axis out the computational domain with an offset  $0.5\delta_x$ . Then the first lattice line is located at  $r = 0.5\delta_x$  and the symmetric boundary conditions can be adopted for the ghost lattice at  $r = -0.5\delta_x$ :

$$\begin{aligned} f_1^*(\mathbf{x}_A, t) &= f_3^*(\mathbf{x}_B, t), & f_5^*(\mathbf{x}_A, t) &= f_6^*(\mathbf{x}_B, t), \\ f_8^*(\mathbf{x}_A, t) &= f_7^*(\mathbf{x}_B, t), \end{aligned} \quad (46)$$

where  $f_i^*$  is the postcollision distribution function. Based on the same mesh rearrangements, David *et al.* [35] proposed a radius-weighted symmetric boundary scheme, in which the values of  $f_i^*$  on the ghost lines are multiplied by  $-1$ :

$$\begin{aligned} f_1^*(\mathbf{x}_A, t) &= -f_3^*(\mathbf{x}_B, t), & f_5^*(\mathbf{x}_A, t) &= -f_6^*(\mathbf{x}_B, t), \\ f_8^*(\mathbf{x}_A, t) &= -f_7^*(\mathbf{x}_B, t). \end{aligned} \quad (47)$$

As for the distribution function  $g_i$ , its equilibrium function is not in a radius-weighted form, and thus only the symmetric boundary schemes can be adopted at the axis.

### A. Flat interface

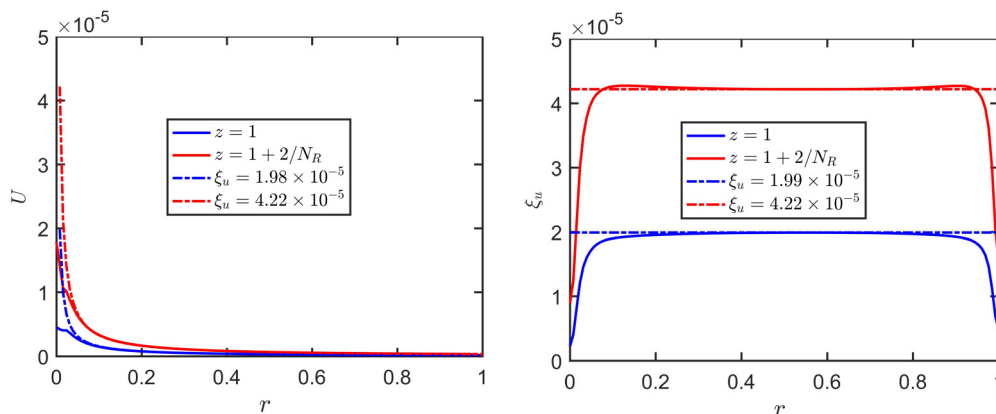
In the first test, the computational domain is a cylinder with radius  $R = 1$  and height  $Z = 2$ , as shown in Fig. 1(a). Initially, a flat interface is located at  $z_c = 1$  and corresponding phase

field can be initialized by its equilibrium state:

$$\phi(r, z) = \frac{\phi_h + \phi_l}{2} + \frac{\phi_h - \phi_l}{2} \tanh\left(\frac{2(z_c - z)}{W/N_R}\right), \quad (48)$$

where  $W = 4$ ,  $\phi_l = 0$ , and  $\phi_h = 1$ . The other parameters are set as  $\rho_h = 1$ ,  $\rho_l = 0.001$ ,  $v_h = v_l = 0.1$ ,  $\sigma = 0.001$ , and  $M_\phi = 0.01$ . For the flat phase interfaces, the mesh size  $N_R \times N_Z$  has no effects on the spurious currents. We adopt a uniform  $128 \times 256$  mesh here. The symmetric boundary condition in Eq. (46) is applied for the postcollision distribution function. Figure 2 presents the time history of the maximum magnitude of velocity  $U_{\max}$  and the kinetic energy  $E = \int 2\pi r \rho |\mathbf{u}|^2 dr dz$ . At the time  $t = 1 \times 10^6$  in the lattice unit,  $U_{\max}$  is on the order of  $O(10^{-5})$  for model I and is reduced to  $O(10^{-8})$  in model II. Both  $U_{\max}$  and  $E$  remain approximately constant in model I at  $t \geq 10^4$ , indicating that the singularity plays an important role in present case and cannot be reduced by increasing the number of iterations.

The magnitude of the spurious current obtained by model I is shown in Fig. 3(a). The maximum unphysical velocity occurs near the intersection of the phase interface and axis. In model II the spurious current is much smaller and uniformly distributed in two separate phases, as shown in Fig. 3(b). According to the macroscopic equation in Eq. (37) and error terms in Eq. (42), the contribution of the singularity is inversely proportional to the radius. Thus, the product of velocity and  $r$  should be approximately constant along the radius coordinate in model I. We introduce the variable  $\xi_u(r, z) = rN_R U(r, z)$  and plot its distribution in Fig. 4. As expected,  $\xi_u$  is uniformly distributed in the  $r$  direction and has a maximum value along the interface, which demonstrates that the peak of velocity in Fig. 3(a) is actually caused by third-order error terms. Variations of  $U$  and  $\xi_u$  along the radius are plotted in Fig. 5. Using  $U = \xi_u/(rN_R)$  as the fitting function, we obtain  $\xi_u = 1.98 \times 10^{-5}$  at  $z = 1$  and  $\xi_u = 4.22 \times 10^{-5}$  at  $z = 1 + 2/N_R$ . Interestingly, the maximum of  $U$  is not located at the interface but is offset by a distance of  $2/N_R$  in the  $z$  direction. Discrepancies between the numerical results and fitted data occur near the axis, indicating that the


 FIG. 5. Distribution of  $U$  and  $\xi_u = rN_R U$  along the radius coordinate at  $z = 1$  and  $z = 1 + 2/N_R$ . Curves obtained through data fitting are shown for comparison.

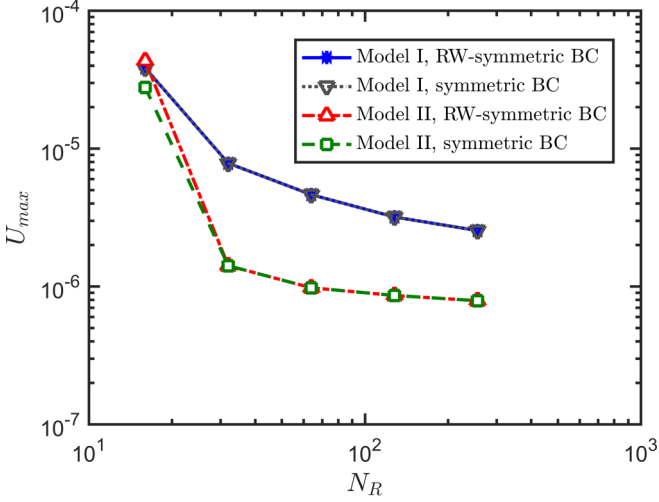


FIG. 6. The effect of mesh size on the maximum spurious current  $U_{\max}$ .

singularity is partially inhibited by the symmetric boundary condition.

It is worth mentioning that a spurious current for the flat interface test is rarely reported. Due to the zero curvature, force balance conditions are often approximately satisfied in most two-phase models, producing small unphysical velocities. Unphysical flows of order  $O(10^{-2})$  near the 2D flat interface have been observed in a finite difference-based LB model [37]. However, as argued by Shan [14], these unphysical flows were caused by an incorrect velocity definition, not discrete errors of imbalanced forces, and they were not spurious currents in the strict sense. To our knowledge, the present study is the first to report a flat interface producing large spurious currents due to third-order truncation error terms.

### B. Spherical interface

To further compare models I and II, we simulated a spherical bubble immersed in a cylindrical domain  $1 \times 2$ . As shown in Fig. 1(b), The bubble is centered at  $(r_c, z_c) = (0, 1)$  and its radius is  $R_0 = 0.5$ . The order parameters for the bubble and liquid are denoted by 0 and 1, respectively. As a result, the

phase field can be initialized by its equilibrium state,

$$\phi(r, z) = \frac{1}{2} + \frac{1}{2} \tanh \left( 2 \frac{\sqrt{(r - r_c)^2 + (z - z_c)^2} - R_0}{W/N_x} \right), \quad (49)$$

where the interface width is  $W = 4$ . The mobility and densities for each phase are fixed at  $M_\phi = 0.01$ ,  $\rho_h = 1$ , and  $\rho_l = 0.001$ . We set  $v_h = v_l = 0.1$  and  $\sigma = 10^{-4}$  to check the effects of grid resolution. As shown in Fig. 6, the maximum of spurious current decreases with  $N_R$  for both models. As  $N_R$  approaches infinity, the circular interface near the axis becomes flat. However, it still suffers from the singular terms based on the discussion in the previous subsection. We also compared the axis boundary conditions for  $f_i$  using Eqs. (46) and (47). No obvious discrepancies were observed between symmetric and RW-symmetric boundary conditions in terms of reducing the spurious current. In the following studies, we use  $128 \times 256$  lattices and RW-symmetric boundary conditions unless specified. The phase field distribution along the axis in the initial and equilibrium states is shown in Fig. 7(a). As can be seen, both models captured the phase interface correctly. The total pressure distribution along the axis is plotted in Fig. 7(b), where the expression for the total pressure  $P$  can be found in Ref. [11]. According to the Laplace law, the pressure difference of two phases should satisfy the relationship  $\Delta P = 2\sigma/R_0$ . The ratios between surface tension calculated by the LB model and the analytical one, i.e.,  $\sigma_{\text{LBM}}/\sigma$ , are 0.9872 and 0.9885 for models I and II, respectively. This good agreement demonstrates that both models can resolve the pressure field accurately.

Next, we examine the effect of surface tension on the spurious current. The viscosity is fixed at  $v_h = v_l = 0.1$ , and the surface tension varies from  $10^{-5}$  to  $10^{-2}$ . As an example, the magnitudes of spurious current for the cases  $\sigma = 10^{-5}$  and  $\sigma = 10^{-2}$  are shown in Fig. 8. As seen, the spurious current is distributed around the phase interface for both models. In model I, the third-order error term produces the singularity of velocity in the region near the axis, which is greatly reduced in model II. For  $\sigma = 10^{-5}$ , periodic fluctuation of the spurious current occurs outside the circle interface, corresponding to eightfold symmetry of the vortex, as previously reported in Ref. [14]. For  $\sigma = 10^{-3}$ , a similar singularity of velocity

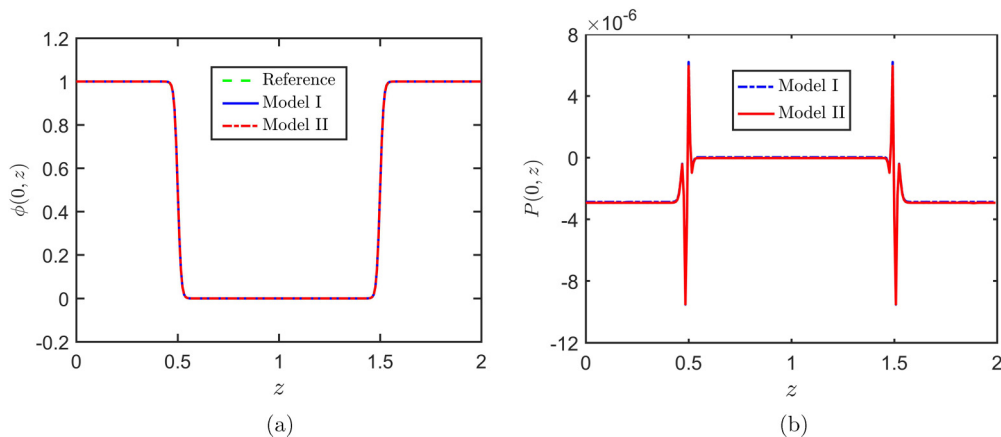


FIG. 7. Comparisons of the phase field and pressure profiles along the axis: (a) phase field profile and (b) pressure profile.



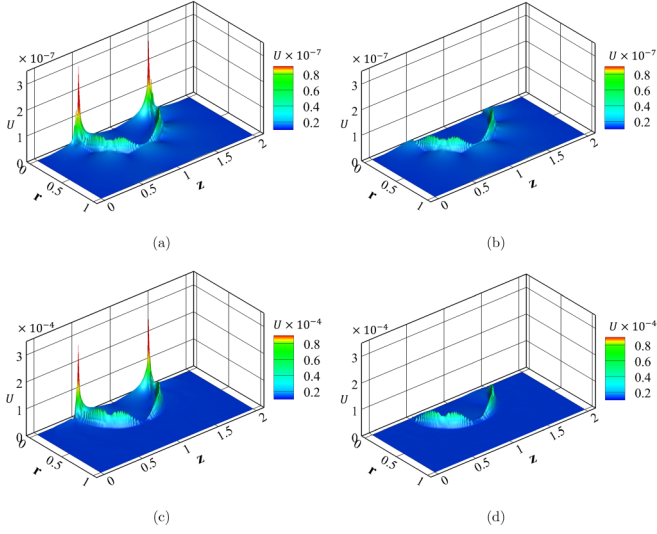


FIG. 8. Magnitude of spurious current distribution by each model at different surface tension values: (a) model I,  $\sigma = 10^{-5}$ ; (b) model II,  $\sigma = 10^{-5}$ ; (c) model I,  $\sigma = 10^{-2}$ ; (d) model II,  $\sigma = 10^{-2}$ .

distribution occurs in model I and can be eliminated by our modified model. Quantitative comparisons of the velocity magnitude at the axis between models I and II are shown in Fig. 9. The maximum spurious current,  $U_{\max}$ , is smaller in model II than model I by two orders of magnitude. In model II the velocity distribution along the axis remains approximately constant, demonstrating elimination of the singularity. The maximum magnitudes of the spurious current for different surface tension values are shown in Fig. 10. Since the maximum values of velocity in model I are located at the axis, we also present the results of model II at  $r = 0$  for better comparison. It can be seen that the maximum magnitudes of the spurious current in model II are always smaller than those in model I among different surface tension values. At the axis, the maximal values of velocity are reduced by our modified model by two orders of magnitude compared with the original RW-LB model. We also note that  $U_{\max}$  is lin-

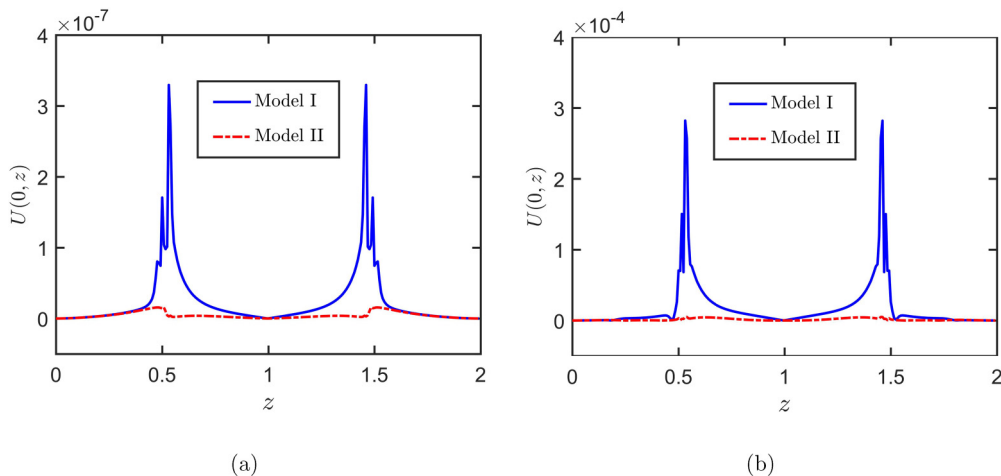


FIG. 9. Magnitude of the spurious current along the axis at surface tension values of (a)  $\sigma = 10^{-5}$  and (b)  $\sigma = 10^{-2}$ .

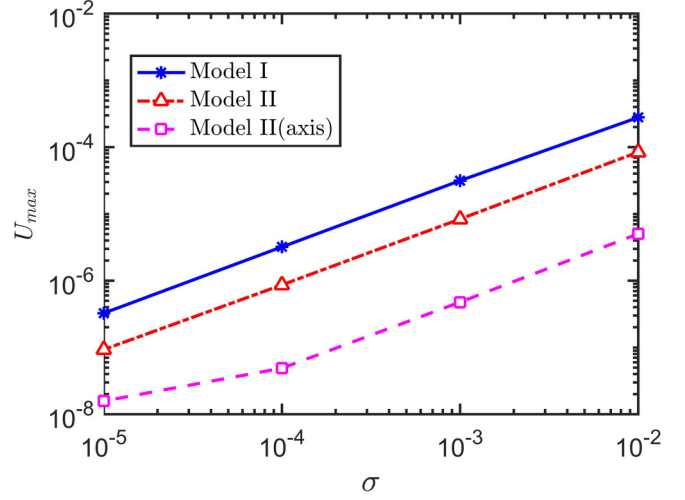


FIG. 10. Relationship between the maximum magnitude of the spurious current and surface tension for models I and II.

early related to  $\sigma$  in both models, which can be explained through the theoretical analysis below. For convenience, we reproduce the recovered macroscopic equation in Eq. (37) as follows:

$$\begin{aligned} r\rho(\partial_t u_\alpha + u_\beta \partial_\beta u_\alpha) = & -\partial_\alpha(rp) + rF_{0\alpha} \\ & + \partial_\beta[r\nu\rho(\partial_\beta u_\alpha + \partial_\alpha u_\beta)] \\ & - 2\rho\nu u_r/r\delta_{\alpha r} + E_\alpha. \end{aligned}$$

The left-hand side of the macroscopic equation is on the order of  $\text{Ma}^2$ , which is neglected in the static bubble test.  $E_\alpha$  can be considered as the discrete error of  $-\partial_\alpha(rp) + rF_{0\alpha} = 0$ . As a result, the spurious currents are produced by  $E_\alpha$  and governed by the simplified relation

$$\partial_\beta[r\nu\rho(\partial_\beta u_\alpha + \partial_\alpha u_\beta)] - 2\rho\nu u_r/r\delta_{\alpha r} + E_\alpha = 0. \quad (50)$$

The definition of chemical potential  $\mu_\phi$  in Eq. (3) indicates that the surface tension force  $\mathbf{F}_s$  is linear to  $\sigma$ . Based on expressions for  $E_\alpha$  in Eq. (38) or Eq. (42), we derive the linear relationship between the spurious current and surface tension.

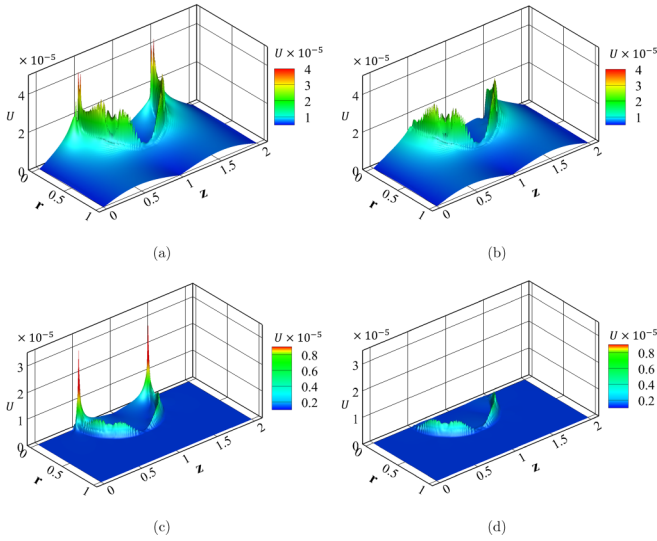


FIG. 11. Magnitude of the spurious current distribution at different viscosity values: (a) model I,  $\nu_h = 0.01$ ; (b) model II,  $\nu_h = 0.01$ ; (c) model I,  $\nu_h = 0.12$ ; (d) model II,  $\nu_h = 0.12$ .

To examine the effect of viscosity, we fix  $\sigma$  at  $10^{-3}$  and adjust  $\nu_h$  from 0.01 to 0.12. Contours of the magnitude of spurious current distribution at  $\nu_h = 0.01$  and  $\nu_h = 0.12$  are shown in Fig. 11. In both cases model II reduces the large spurious current near the intersection of the axis and phase interface. At  $\nu_h = 0.01$ , a larger magnitude and wider distribution of the spurious current are observed. The magnitudes of the spurious current at singularities have a comparable value with that far from the axis, indicating that the viscosity ratio plays an equivalent important role in spurious current formation. We compare the magnitude of the spurious current along the axis obtained by models I and II in Fig. 12. At  $\nu_h = 0.01$ , the maximum spurious current in model II is about one third that for model I. Although the third-order terms producing the singularity have been removed, large spurious currents remain near intersections of the phase field and axis. At  $\nu_h = 0.12$ , the magnitude of the spurious current at the axis is reduced by two orders of magnitude in model II. The maximum magnitude of the spurious current with different viscosity are summarized

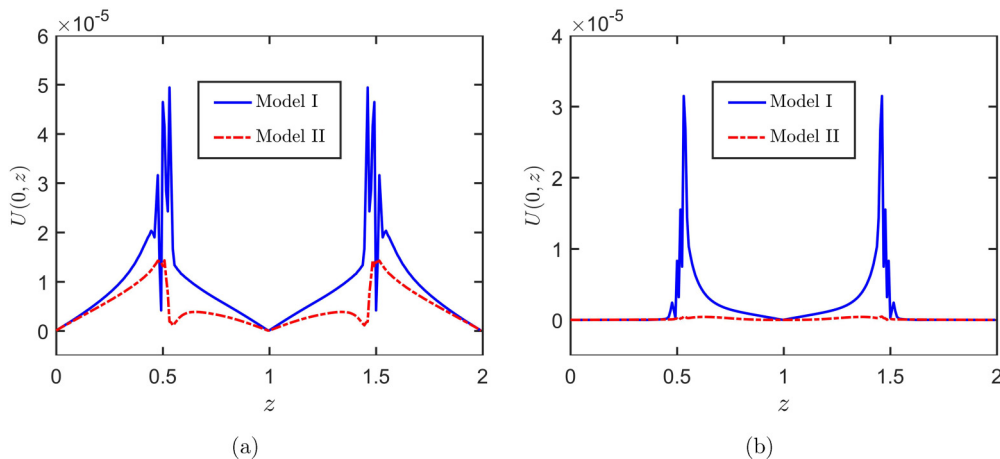


FIG. 12. Magnitude of the spurious current along the axis for viscosity values of (a)  $\nu_h = 0.01$  and (b)  $\nu_h = 0.12$ .

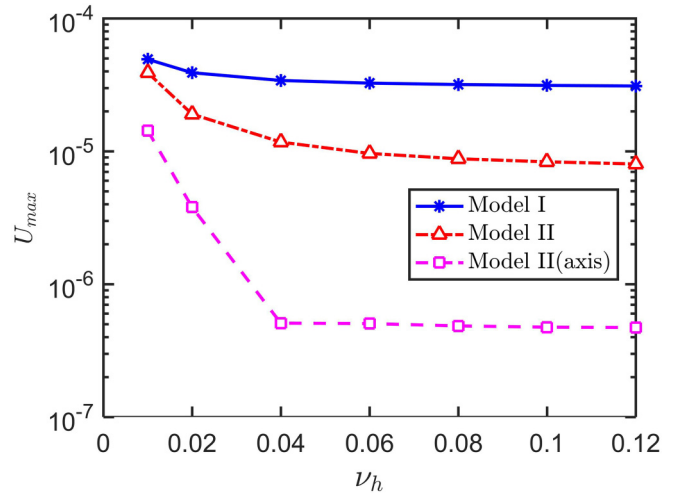


FIG. 13. Relationship between the maximum magnitude of the spurious current and viscosity for models I and II.

in Fig. 13. Again the maximum magnitudes of velocity at the axis in model I are also plotted for comparison. The  $U_{\max}$  values in our modified model are consistently lower than those for model I, and the gap widens as  $\nu_h$  increases. At  $0.04 \leq \nu_h \leq 0.12$ , the effect of  $\nu_h$  on the spurious current is very small. At  $\nu_h < 0.4$ , the values of  $U_{\max}$  increases rapidly as  $\nu_h$  decreases, indicating balance force conditions are hard to achieve at small kinematic viscosity ratios.

### C. Rising bubble

To check the validity of our model in capturing realistic phase interfaces, we conduct a single rising bubble simulation and compare with corresponding experimental and numerical results [38–40]. The buoyancy-driven bubble is one of the most common gas-liquid flow phenomena. A fundamental understanding of the bubble dynamics is essential for many industrial applications such as gas-liquid column reactors [41] and microfluidic devices [42]. Extensive experimental and numerical studies have been performed to investigate the motion and deformation of a rising bubble in a viscous liquid.

TABLE I. Dimensionless numbers and parameter settings for different cases.

Case	Mo	Bo	$g$	$\sigma$	Shape regime
A	711	17.7	$1 \times 10^{-6}$	$2.31 \times 10^{-4}$	Spherical
B	$8.2 \times 10^{-4}$	32.2	$4 \times 10^{-6}$	$5.08 \times 10^{-4}$	Ellipsoidal
C	266	243	$4 \times 10^{-6}$	$6.74 \times 10^{-5}$	Dimpled ellipsoidal cap
D	$4.63 \times 10^{-3}$	115	$8 \times 10^{-6}$	$2.85 \times 10^{-4}$	Spherical cap

Theoretically, the bubble dynamics are governed by four independent dimensionless parameters: the density ratio  $\lambda_\rho = \rho_h/\rho_l$ , viscosity ratio  $\lambda_\mu = \mu_h/\mu_l$ , Bond number,

$$Bo = \frac{\rho_h g d_0^2}{\sigma}, \tag{51}$$

and Morton number,

$$Mo = \frac{g \mu_h^4}{\rho_h \sigma^3}, \tag{52}$$

where  $d_0$  is the bubble diameter,  $g$  is the magnitude of gravitational acceleration, and  $\mu_{h/l}$  is the viscosity for the liquid or bubble phase. In addition, the Reynolds number (Re) are commonly used to describe the steady motion,

$$Re = \frac{\rho_h U_t d_0}{\mu_h}, \tag{53}$$

where  $U_t$  is the terminal velocity of the bubble.

In our LB simulation, the ratios of density and viscosity are fixed at  $\lambda_\rho = 1000$  and  $\lambda_\mu = 100$ , which correspond to the parameters in a air-water system. Initially, a spherical gas bubble is placed on the axis at  $4d_0$  above the bottom of a cylindrical cavity. The size of the computational domain is set as  $4d_0 \times 16d_0$  so that effects of the lateral and top walls can be neglected. The buoyancy force in the vertical direc-

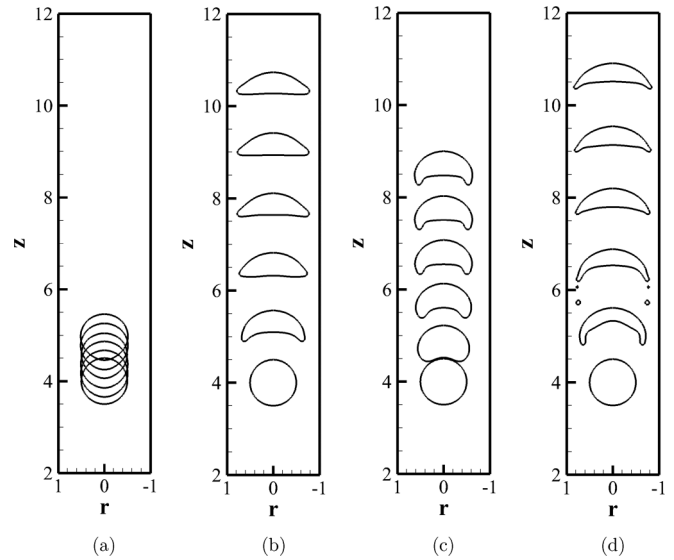
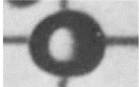
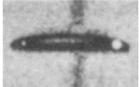
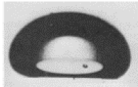
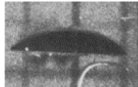














FIG. 14. Temporal evolution of the bubble interfaces with a time interval of  $\Delta \bar{t} = 2$ . Contours from left to right correspond to (a) case A, (b) case B, (c) case C, and (d) case D, respectively.

tion is given by  $F_{bz} = (\rho_h - \rho)g$ . The dimensionless time is defined by  $\bar{t} = t\sqrt{g/d_0}$ . We set  $d_0 = 64$  in lattice units and thus have a uniform grid of resolution  $256 \times 1024$ , which is fine enough to obtain grid-independent results. The mobility parameter and interface width are  $M_\phi = 0.1$  and  $W = 4$ , respectively. Both liquid and bubble phases are assumed quiescent at  $t^* = 0$ . The phase field and density are initialized according to Eqs. (2) and (11). Axial symmetric boundary conditions are used at  $r = 0$ , while half-way bounce-back boundary conditions are adopted for other sides. Four cases with different values of Bo and Mo are tested. Detailed lattice parameter settings are given in Table I, and corresponding physical parameters can be found in Ref. [40]. We set  $\rho_h = 1$  and  $\rho_l = 0.001$  in the present studies. Once the value of  $g$  is

TABLE II. Terminal bubble shapes and Reynolds number compared with experimental tests [38] and numerical results in literature [39,40].

Case	Case A	Case B	Case C	Case D
Experiments [38]	 Re = 0.232	 Re = 55.3	 Re = 7.77	 Re = 94.0
3D LSM [40]	 Re = 0.172	 Re = 51.86	 Re = 7.86	 Re = 87.6
Axisymmetric FTM [39]	 Re = 0.194	 Re = 52.96	 Re = 8.4	 Re = 88.7
Present work	 Re = 0.172	 Re = 52.40	 Re = 7.36	 Re = 90.04

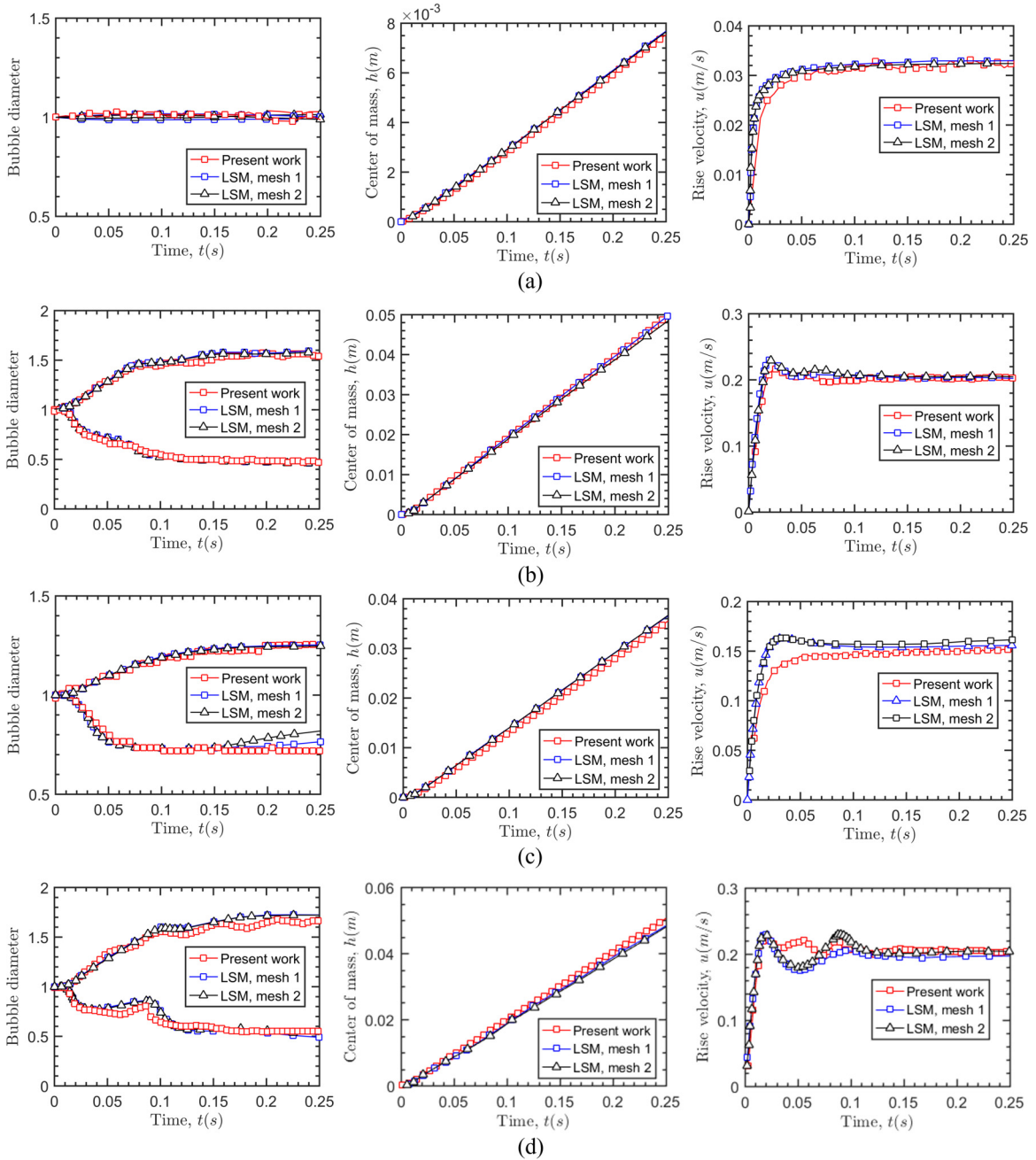


FIG. 15. Temporal evolution of the bubble rising parameters for different cases: (a) case A, (b) case B, (c) case C, and (d) case D. Curves from left to right represent the variation with time of the bubble diameter, center of mass, and rise velocity, respectively.

specified, other unknown parameters can be determined based on Eqs. (51) and (52).

Figure 14 presents the temporal evolution of bubble shapes at a time interval of  $\Delta \bar{t} = 2$ . At  $\bar{t} = 10$ , all cases reach their steady states. The bubble for case A moves slowly and almost maintains its initial spherical shape during the rising process. As  $Bo$  increases, the role of surface tension becomes weak, and the bubble tends to undergo large deformation. In cases B, C, and D, the terminal bubble shapes are ellipsoidal, dimpled ellipsoidal cap, and spherical cap, respectively. Following Ref. [40], we plot the bubble diameter, center of mass, and rising velocity as a function of time for different cases in Fig. 15. Compared with the 3D level-set method (LSM) [40], good

agreements are achieved by our axisymmetric LB method. Some slight differences between them may originate from different mesh sizes and different interface-capturing approaches adopted. In Table II we compare the terminal bubble shapes and Reynolds numbers with experiments reported by Bhaga and Weber [38], and numerical predictions using the axisymmetric front-tracking method (FTM) [40] and 3D level-set method. The bubble shapes obtained by our modified model are consistent with those experimental and numerical results. Quantitative comparison of the Reynolds numbers also shows quite good agreements. The slight discrepancy between the experiments and numerical simulation can be attributed to the experimental uncertainties and numerical errors. The

experimental uncertainties include measurement errors, initial shape perturbations, and effects of surfactants. The numerical errors mainly come from the 3D effects, the discretization errors, and the assumption of spherical shape and stagnant flow for the initial conditions. Even so, it can be demonstrated from Table II that the present axisymmetric lattice Boltzmann model can properly capture single bubble dynamics in a viscous fluid.

## VI. CONCLUSION

In this study severe spurious currents near the axis in the RW-LB model were shown to be caused by singularity of the error terms through high-order Taylor series expansion. Dimensionless analysis was used to obtain the leading error terms at the third order. We carefully designed an appropriate source term to develop a modified model that eliminates the singularity of the RW-LB model. This additional source term is very simple and can be implemented locally. The modified model was validated for flat and spherical interfaces; the results showed that the modified model reduced the spurious currents near the axis by two orders of magnitude compared with the original RW-LB model for most cases. These spurious currents in our modified model may be further decreased using multiple-relaxation-time (MRT) collision operators [43] or high-order differential schemes for derivatives of the order parameter [11]; however, these additional modifications are beyond the scope of this study. Although the correction term implemented in our modified model is designed for the phase-field-based RW-LB model, it can be directly extended to other types of RW-LB models, e.g., a free-energy-based model, for multiphase or multicomponent flows.

## ACKNOWLEDGMENTS

This work was funded by the National Key R&D Program of China (Grant No. 184 2020YFA0709700) and the Key Project of National Natural Science Foundation of China (Grant No. 52032004).

## APPENDIX A: CHAPMAN-ENSKOG ANALYSIS OF AXISYMMETRIC LB MODEL FOR THE ALLEN-CAHN EQUATION

Second-order Taylor series expansion of the evolution equation, Eq. (5), yields

$$D_t h_i + \frac{\delta_t}{2} D_i^2 h_i = -\frac{h_i - h_i^{\text{eq}}}{\tau_m \delta_t} + \left(1 - \frac{1}{2\tau_m}\right) H_i. \quad (\text{A1})$$

Through the Chapman-Enskog expansion, the following multiscale expansions are introduced:

$$\begin{aligned} \partial_t &= \varepsilon \partial_{t1} + \varepsilon^2 \partial_{t2}, & \partial_\alpha &= \varepsilon \partial_{1\alpha}, \\ h_i &= h_i^{(0)} + \varepsilon h_i^{(1)} + \varepsilon^2 h_i^{(2)} + \dots, & H_i &= \varepsilon H_i^{(1)}. \end{aligned} \quad (\text{A2})$$

Substituting these expansions into Eq. (A1), the evolution equation can be reorganized in consecutive orders of  $\varepsilon$  as

$$\varepsilon^0: h_i^{(0)} = h_i^{\text{eq}}, \quad (\text{A3a})$$

$$\varepsilon^1: D_{1i} h_i^{(0)} = -\frac{h_i^{(1)}}{\tau_m \delta_t} + \left(1 - \frac{1}{2\tau_m}\right) H_i^{(1)}, \quad (\text{A3b})$$

$$\varepsilon^2: \partial_{t2} h_i^{(0)} + D_{1i} h_i^{(1)} + \frac{\delta_t}{2} D_{1i}^2 h_i^{(0)} = -\frac{1}{\tau_m \delta_t} h_i^{(2)}, \quad (\text{A3c})$$

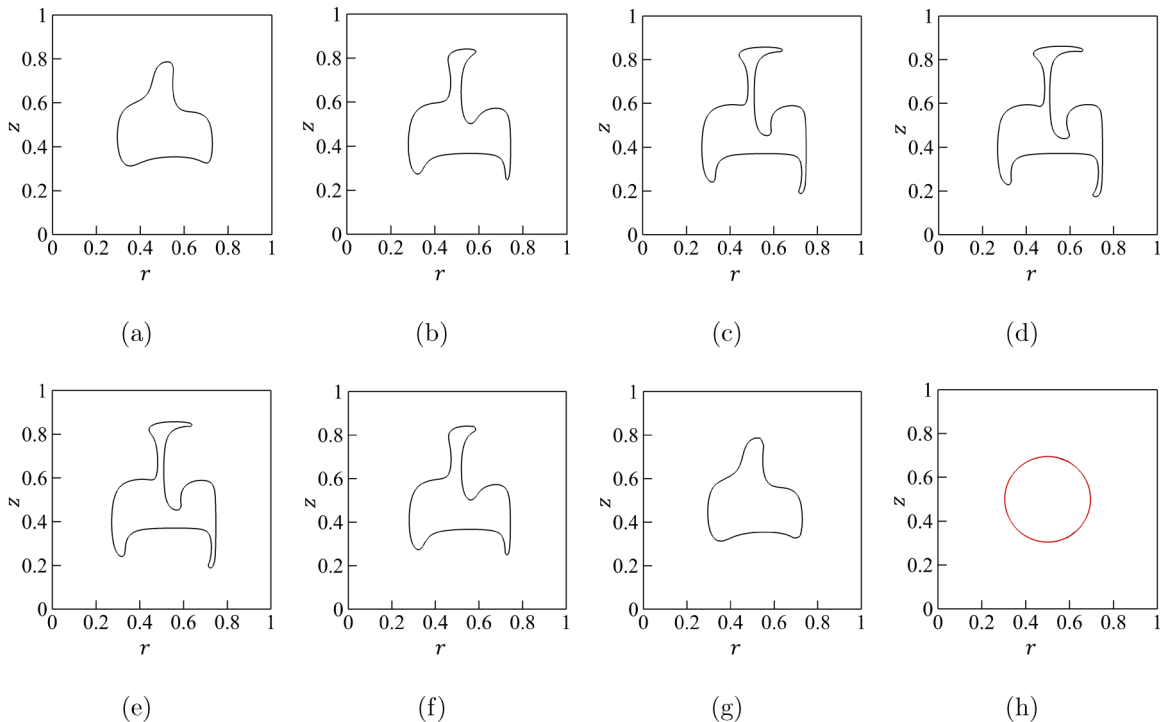


FIG. 16. Phase interfaces obtained at (a)  $t = T/8$ , (b)  $t = T/4$ , (c)  $t = 3T/8$ , (d)  $t = T/2$ , (e)  $t = 5T/8$ , (f)  $t = 3T/4$ , (g)  $t = 7T/8$ , and (h)  $t = 0$  (red line) and  $t = T$  (black line).



where  $D_{1i} = \partial_{r1} + e_{i\alpha}\partial_{1\alpha}$ . Substituting Eq. (A3b) in Eq. (A3c) gives

$$\begin{aligned} \varepsilon^2: \partial_{t2}h_i^{(0)} + D_{1i} \left[ \left(1 - \frac{1}{2\tau_m}\right) (h_i^{(1)} + 0.5\delta_t H_i^{(1)}) \right] \\ = -\frac{1}{\tau_m\delta_t} h_i^{(2)}. \end{aligned} \quad (\text{A4})$$

The moments of the equilibrium distribution function and source term are expressed as  $\sum_i h_i^{\text{eq}} = \phi$ ,  $\sum_i e_{i\alpha} h_i^{\text{eq}} = \phi u_\alpha$ ,  $\sum_i e_{i\alpha} e_{i\beta} h_i^{\text{eq}} = c_s^2 \phi \delta_{\alpha\beta} + \phi u_\alpha u_\beta$ ,  $\sum_i H_i^{(1)} = -\phi u_r/r$ , and  $\sum_i e_{i\alpha} H_i^{(1)} = c_s^2 \theta n_\alpha$ . From Eq. (10) and Eq. (A3a), we can derive  $\sum_i h_i^0 = \phi$ ,  $\sum h_i^{(1)} = 0.5\delta_t \phi u_r/r$  and  $\sum h_i^{(2)} = 0$ . Taking summation of Eq.(A3b) and Eq.(A4) over  $i$ , we obtain the following equation:

$$\partial_{t1}\phi + \partial_{1\alpha}(\phi u_\alpha) = -\phi u_r/r, \quad (\text{A5a})$$

$$\partial_{t2}\phi + \partial_{1\alpha}P_\alpha^{(1)} = 0, \quad (\text{A5b})$$

where  $P_\alpha^{(1)}$  is calculated by

$$\begin{aligned} P_\alpha^{(1)} &= (\tau_m - 0.5)\delta_t \sum_i e_{i\alpha} (H_i^{(1)} - D_{1i}h_i^{(0)}) \\ &= (\tau_m - 0.5)\delta_t [c_s^2 \theta n_\alpha - \partial_{t1}(\phi u_\alpha) - c_s^2 \partial_\alpha \phi - \partial_\beta(\phi u_\beta u_\alpha)]. \end{aligned} \quad (\text{A6})$$

Combining Eq. (A5a) and Eq. (A5b), the macroscopic equation can be recovered as

$$\partial_t \phi + \partial_\alpha(\phi u_\alpha) + \frac{\phi u_r}{r} = \partial_\alpha [M_\phi(\partial_\alpha \phi - \theta n_\alpha)] + E^\phi, \quad (\text{A7})$$

where the error terms  $E^\phi = \frac{M_\phi}{c_s^2} [\partial_{t\alpha}(\phi u_\alpha) + \partial_{\alpha\beta}(\phi u_\alpha u_\beta)]$  are on the order of  $O(\text{Ma}^2)$  and are therefore negligible in the present studies. At large Mach number, the error terms can be eliminated by adding a correction term [12], modify-

ing the collision process [44], or adopting a modified MRT scheme [21,45].

## APPENDIX B: BENCHMARK TEST FOR THE ALLEN-CAHN EQUATION

To evaluate the performance of our LB model for the Allen-Cahn equation in capturing the complex interface, we design a benchmark test analogous to the 2D drop test in shear flow [46]. The cylindrical computational domain is set as  $N_R = N_Z = 512$ . A 2D axisymmetric circular bubble with radius 100 is located at (256, 256). The rotational velocity field is given by the stream function equation, as follows:

$$\psi = \frac{U_0}{n\pi} [r^2 \sin(n\pi r) \cos(n\pi z)] \cos \frac{\pi t}{T}. \quad (\text{B1})$$

Thus, the velocity can be obtained from  $u = \frac{1}{r} \frac{\partial \psi}{\partial z}$ ,  $v = -\frac{1}{r} \frac{\partial \psi}{\partial r}$ ,

$$\begin{bmatrix} u \\ v \end{bmatrix} = -U_0 \begin{bmatrix} r \sin(n\pi r) \times \sin(n\pi z) \\ \left[ \frac{2\sin(n\pi r)}{n\pi} + r \cos(n\pi r) \right] \times \cos(n\pi z) \end{bmatrix} \cos \frac{\pi t}{T}, \quad (\text{B2})$$

where the period time is  $T = 1.25N_R/U_0$ . Other parameters are set as  $n = 4$ ,  $U_0 = 0.01$ ,  $W = 4$ , and  $M_\phi = 0.005$ . The left and right boundaries are enforced by symmetric boundary conditions. The vertical boundaries are periodic. The phase interface evolution during one period is shown in Fig. 16, where the computational domain length is scaled by  $N_R$ . The circle is stretched and spiraled during the first half period and reaches the maximum deformation at  $t = T/2$ . Subsequently, the phase interface moves in the opposite direction and returns to its initial state at time  $T$ . Unlike the behavior of a 2D drop in shear flow (Fig. 9 in Ref. [46]), the symmetry of the phase interface is broken for the axisymmetric case. In Fig. 16(h) the final phase interface profile is in a good agreement with its initial state (denoted by red line). The relative error of the phase field is  $6.91 \times 10^{-4}$ , and the relative volume change for the bubble is  $-2.05 \times 10^{-5}$ . We conclude that our modified model for an axisymmetric Allen-Cahn equation is able to not only obtain a stable and accurate interface but also guarantee the mass conservation.

- 
- [1] Y. Peng, C. Shu, Y. T. Chew, and J. Qiu, *J. Comput. Phys.* **186**, 295 (2003).  
[2] I. Halliday, L. A. Hammond, C. M. Care, K. Good, and A. Stevens, *Phys. Rev. E* **64**, 011208 (2001).  
[3] T. Reis and T. N. Phillips, *Phys. Rev. E* **75**, 056703 (2007).  
[4] J. G. Zhou, *Phys. Rev. E* **78**, 036701 (2008).  
[5] Q. Li, Y. L. He, G. H. Tang, and W. Q. Tao, *Phys. Rev. E* **81**, 056707 (2010).  
[6] J. G. Zhou, *Phys. Rev. E* **84**, 036704 (2011).  
[7] Z. Guo, H. Han, B. Shi, and C. Zheng, *Phys. Rev. E* **79**, 046708 (2009).  
[8] L. Zhang, S. Yang, Z. Zeng, J. Chen, L. Wang, and J. W. Chew, *Comput. Math. Appl.* **74**, 817 (2017).  
[9] L. Zheng, Z. Guo, B. Shi, and C. Zheng, *J. Comput. Phys.* **229**, 5843 (2010).  
[10] Y. Huo and Z. Rao, *Int. J. Heat Mass Transf.* **119**, 1 (2018).  
[11] H. Liang, Z. H. Chai, B. C. Shi, Z. L. Guo, and T. Zhang, *Phys. Rev. E* **90**, 063311 (2014).  
[12] H. Liang, Y. Li, J. Chen, and J. Xu, *Int. J. Heat Mass Transf.* **130**, 1189 (2019).  
[13] S. Leclaire, M. Reggio, and J. Trépanier, *Comput. Fluids* **48**, 98 (2011).  
[14] X. Shan, *Phys. Rev. E* **73**, 047701 (2006).  
[15] Z. Yu and L. Fan, *J. Comput. Phys.* **228**, 6456 (2009).  
[16] M. R. Swift, W. R. Osborn, and J. M. Yeomans, *Phys. Rev. Lett.* **75**, 830 (1995).  
[17] H. Huang, J. J. Huang, and X. Y. Lu, *J. Comput. Phys.* **269**, 386 (2014).  
[18] Y. Wang, C. Shu, H. Huang, and C. Teo, *J. Comput. Phys.* **280**, 404 (2015).  
[19] A. Fakhari, M. Geier, and T. Lee, *J. Comput. Phys.* **315**, 434 (2016).

- [20] A. Fakhari, D. Bolster, and L. Luo, *J. Comput. Phys.* **341**, 22 (2017).
- [21] X. Xu, Y. Hu, B. Dai, L. Yang, J. Han, Y. He, and J. Zhu, *Phys. Rev. E* **104**, 035305 (2021).
- [22] K. Connington and T. Lee, *J. Mech. Sci. Technol.* **26**, 3857 (2012).
- [23] A. J. Wagner, *Int. J. Mod. Phys. B* **17**, 193 (2003).
- [24] T. Seta and K. Okui, *J. Fluid Sci. Technol.* **2**, 139 (2007).
- [25] C. M. Pooley and K. Furtado, *Phys. Rev. E* **77**, 046702 (2008).
- [26] T. Lee and P. F. Fischer, *Phys. Rev. E* **74**, 046709 (2006).
- [27] Z. Guo, C. Zheng, and B. Shi, *Phys. Rev. E* **83**, 036707 (2011).
- [28] Z. Guo, *Phys. Fluids* **33**, 031709 (2021).
- [29] A. Begmohammadi, R. Haghani-Hassan-Abadi, A. Fakhari, and D. Bolster, *Phys. Rev. E* **102**, 023305 (2020).
- [30] J. Kim, *J. Comput. Phys.* **204**, 784 (2005).
- [31] M. Geier, A. Fakhari, and T. Lee, *Phys. Rev. E* **91**, 063309 (2015).
- [32] A. Fakhari, T. Mitchell, C. Leonardi, and D. Bolster, *Phys. Rev. E* **96**, 053301 (2017).
- [33] T. Lee and L. Liu, *J. Comput. Phys.* **229**, 8045 (2010).
- [34] D. J. Holdych, D. R. Noble, J. G. Georgiadis, and R. O. Buckius, *J. Comput. Phys.* **193**, 595 (2004).
- [35] D. David, F. Kuznik, K. Johannes, and L. Merlier, *Comput. Fluids* **116**, 46 (2015).
- [36] Q. Zhai, L. Zheng, and S. Zheng, *Phys. Rev. E* **95**, 023313 (2017).
- [37] A. Cristea and V. Sofonea, *Int. J. Mod. Phys. C* **14**, 1251 (2003).
- [38] D. Bhaga and M. Weber, *J. Fluid Mech.* **105**, 61 (1981).
- [39] J. Hua and J. Lou, *J. Comput. Phys.* **222**, 769 (2007).
- [40] M. Grave, J. J. Camata, and A. L. Coutinho, *Comput. Fluids* **209**, 104667 (2020).
- [41] N. Kantarci, F. Borak, and K. O. Ulgen, *Process Biochem.* **40**, 2263 (2005).
- [42] C.-X. Zhao and A. P. Middelberg, *Chem. Eng. Sci.* **66**, 1394 (2011).
- [43] Z. Yu and L. S. Fan, *Phys. Rev. E* **82**, 046708 (2010).
- [44] H. Zheng, C. Shu, and Y. Chew, *J. Comput. Phys.* **218**, 353 (2006).
- [45] R. Huang and H. Wu, *J. Comput. Phys.* **274**, 50 (2014).
- [46] H. Liang, B. C. Shi, Z. L. Guo, and Z. H. Chai, *Phys. Rev. E* **89**, 053320 (2014).